Article

Superluminal correlations in ensembles of optical phase singularities

https://doi.org/10.1038/s41586-026-10209-z

Received: 22 September 2025

Accepted: 28 January 2026

Published online: 25 March 2026

Check for updates

T. Bucher[1,12], A. Gorlach[1,12], A. Niedermayr[1], Q. Yan[1], H. Nahari[1], K. Wang[2], R. Ruimy[1], Y. Adiv[1], M. Yannai[1], T. L. Abudi[1], E. Janzen[3], C. Spaegele[4], C. Roques-Carmes[5], J. H. Edgar[3], F. H. L. Koppens[6,7], G. M. Vanacore[8], H. H. Sheinfux[9], S. Tsesses[1,10] & I. Kaminer[1,11] ✉

Phase singularities—points carrying quantized topological charge—are universal features found across diverse wave systems from superfluids and superconductors to acoustic and optical fields[1–4]. Ensembles of these singularities exhibit distance correlations resembling particles in liquids[5–8], extensively studied for their role in exotic material phases[9–11]. By contrast, the full correlations in phase space that govern the system evolution have remained unexplored and experimentally inaccessible. Here we directly measure the ultrafast dynamics of optical singularity ensembles, capturing their full phase-space correlations, presenting the joint distance–velocity distribution. Our observations show a breakdown of the particle-singularity analogy[12]: phase singularities accelerate towards formally divergent velocities in the moment before annihilation[7,13,14], indicated by measurements of velocities exceeding the speed of light. These apparent superluminal velocities are paradoxically amplified by the slow group velocity of hyperbolic phonon polaritons in our material platform, hexagonal boron nitride membranes[15–19]. We demonstrate these phenomena using combined hardware and algorithmic advances in ultrafast electron microscopy[18,20–25], achieving spatial and temporal resolutions, each an order of magnitude below the polaritonic wavelength and cycle period. Our findings deepen our understanding of phase singularities and their universality, enabling to probe topological defect dynamics at previously unattainable timescales.

Singularities of many kinds arise in nearly every branch of physics, from dislocations in crystals[9] and flux quanta in superconductors[1] to vortex cores in fluid flows (for example, cyclones) and quantized vortices in superfluids[2]. Other manifestations are ubiquitous in materials supporting optical, phononic and plasmonic wave fields[3]. The understanding of singularities has roots in the 1885 'hairy ball theorem', and has vastly evolved ever since, particularly in the context of singular optics[4,26,27]. Optical singularities enable precise control of light–matter interactions with both bound and free electrons[28,29], underpin super-resolution imaging[30,31] and encode classical and quantum information[32,33] that can be imprinted on the orbital angular momentum carried by the field surrounding the singularity. These opportunities motivate extensive research into generating and imaging singularities, continually showing their fundamental properties across a wide range of optical systems[11,34,35].

Another reason for the interest in singularities in wave systems is the strong analogy between phase singularities and interacting particles. The particle-singularity analogy arises because of the stable nature of phase singularities carrying topological charge ±1, characterized by a ±2π phase winding. Rare singularity events could, in principle, carry higher integer topological charges, but they are typically unstable[36,37]. Similar to particle–antiparticle pairs, a singularity annihilates only when encountering another singularity of the opposite charge. This analogy is regarded as a manifestation of wave–particle duality in classical systems[5,12,26].

When dealing with many such singularities, that is, singularity ensembles, their collective statistics and correlations become crucial for understanding the global system properties[10]. The distance correlations resemble those of interacting particles that make up liquids, independently of the true underlying physics of the singularities. Pioneering experiments observed these distance correlations in microwave[38] and optical[6] domains. These and other studies focused on the distance-correlation functions in singularity ensembles, following Berry's foundational work on their statistical properties[5] and later works on singularity-pair correlations[7].

Extensive theoretical efforts have also been dedicated to analysing the dynamics of singularity ensembles under temporal evolution[7,13,14,27], including the prediction of their velocity distributions[7].

[1]Andrea and Erna Viterbi Department of Electrical and Computer Engineering, Technion–Israel Institute of Technology, Haifa, Israel. [2]Shanghai Institute of Optics and Fine Mechanics, Chinese Academy of Sciences, Shanghai, China. [3]Tim Taylor Department of Chemical Engineering, Kansas State University, Manhattan, KS, USA. [4]Harvard John A. Paulson School of Engineering and Applied Sciences, Harvard University, Cambridge, MA, USA. [5]E. L. Ginzton Laboratory, Stanford University, Stanford, CA, USA. [6]ICFO-Institut de Ciències Fotòniquses, The Barcelona Institute of Science and Technology, Castelldefels, Spain. [7]ICREA-Institució Catalana de Recerca i Estudis Avancats, Barcelona, Spain. [8]Department of Materials Science, University of Milano-Bicocca, Milano, Italy. [9]Department of Physics, Bar-Ilan University, Ramat Gan, Israel. [10]Department of Physics, MIT-Harvard Center for Ultracold Atoms and Research Laboratory of Electronics, Massachusetts Institute of Technology, Cambridge, MA, USA. [11]Faculty of Materials Science and Engineering, Technion–Israel Institute of Technology, Haifa, Israel. [12]These authors contributed equally: T. Bucher, A. Gorlach. ✉e-mail: kaminer@technion.ac.il

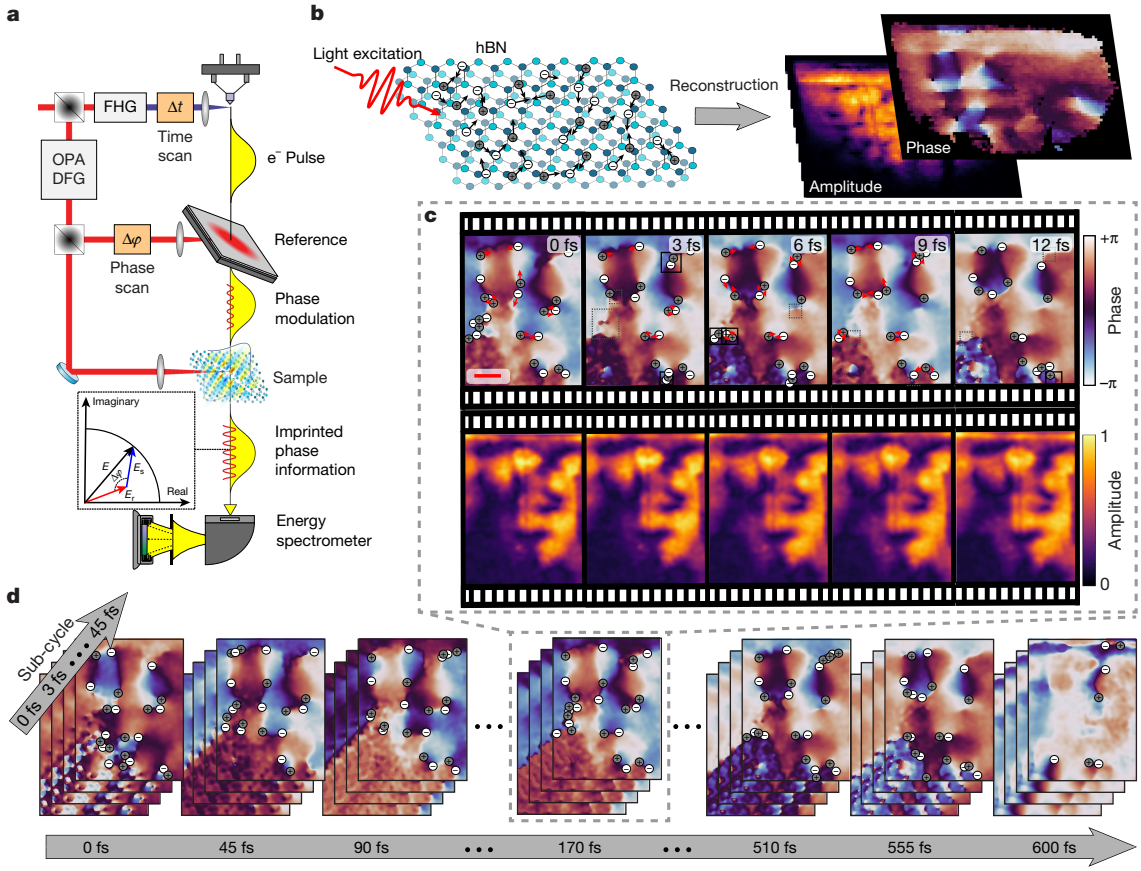

Fig. 1 | Deep sub-wavelength and deep sub-cycle imaging of optical phase singularities in hBN, recording both phase and group dynamics. **a**, A femtosecond laser pulse is split into three parts to excite the electron pulse, modulate it at the reference and create PhPs in the sample. By timing the pulses, we record the phase ($\Delta\phi$) and group dynamics (Δt). **b**, The spatiotemporal dynamics of singularities and their phase-space correlations are measured in hBN, extracting their phase and amplitude. **c**, Measured phase dynamics of singularities show sub-cycle creation and annihilation events. Scale bar, 3 µm. **d**, The entire measurement (see also Supplementary Information movie) captures both deep sub-cycle (3 fs) and group dynamics (>800 fs) of singularities, with deep sub-wavelength resolution (20 nm) over a macroscopic field of view ($21 \times 21\ \mu m^2$). These constitute deep sub-wavelength phase imaging (×350 below the free-space wavelength and roughly ×30 below the PhP wavelength), with deep sub-cycle temporal resolution (×8 below the cycle time).

However, experimental research has lagged behind theory. Observing the dynamics of singularities requires measuring the optical (or quantum) system with a sub-cycle, sub-wavelength resolution, which is a substantial technical challenge.

Remarkable phenomena in optical singularity dynamics remain hidden, both at the level of individual singularities and within their collective ensembles[26]. Most notably, theory has long predicted that optical singularities exhibit heavy-tailed statistics, containing extreme events of apparent superluminal motion (singularities exceed the speed of light without breaking causality). Particularly at moments close to singularity-pairs creation or annihilation, their velocities can become divergent[7,13,14,27].

Here, we monitor the ultrafast dynamics of optical phase singularities with deep sub-wavelength spatial and deep sub-cycle temporal resolutions, revealing their acceleration near annihilation events. Quantitative analysis of the singularity velocities shows points in space and time in which the velocities of certain singularities surpass the velocity of light, c. We explore the ultrafast dynamics of the singularities by both direct observation of individual annihilation events and using large-scale statistical analysis in the phase space of their position and velocity, captured by distance–velocity correlations among all singularity pairs. The measured distance correlations support the well-known particle-like nature of singularities, whereas their velocity distribution pinpoints the breakdown of the particle analogy by distinct heavy-tailed statistics, apparent superluminal speeds and sub-cycle creation and annihilation events.

Deep sub-wavelength and sub-cycle singularity mapping

The key findings emerge from reaching deep sub-wavelength phase imaging (20 nm ≈ $\lambda_{PhP}/30$), with deep sub-cycle temporal resolution (3 fs ≈ $T/8$), over a large field of view and long overall measurement duration. This experiment is performed on an optical platform of hyperbolic phonon-polariton (PhP) wavepackets in a thin hexagonal boron nitride (hBN) flake[15,39], using an ultrafast transmission electron microscope (UTEM)[20,21]. We rely on the photon-induced near-field electron microscopy (PINEM) technique[20,22] extended to resolve the field phase[23–25] by free-electron Ramsey imaging (FERI)[25], providing unambiguous identification of the singularity charge. We use mid-infrared femtosecond pulses (average wavelength $\lambda_0 = 7$ µm, corresponding to a field cycle of $T = 23.3$ fs) to create PhP wavepackets. Because of the hyperbolic dispersion characteristic of PhPs[15], they can be confined to sub-wavelength dimensions, in our experiments on the order of $\lambda_{PhP} \approx \lambda_0/11 \approx 630$ nm. The hyperbolic dispersion also leads to a slow group velocity, reaching more than 100 times slower than the speed of light[16–18]. Furthermore, PhPs exhibit remarkably low optical losses, especially for isotopically pure hBN, for which the PhP lifetime can reach well over a picosecond[19]. The combination of all these factors, with the advance of phase-resolved polariton imaging in electron microscopy, makes hBN a favourable platform to observe universal properties of singularity dynamics.

Each iteration of the experiment begins by dividing the near-infrared pulse into three paths (Fig. 1a). The first path is upconverted to the

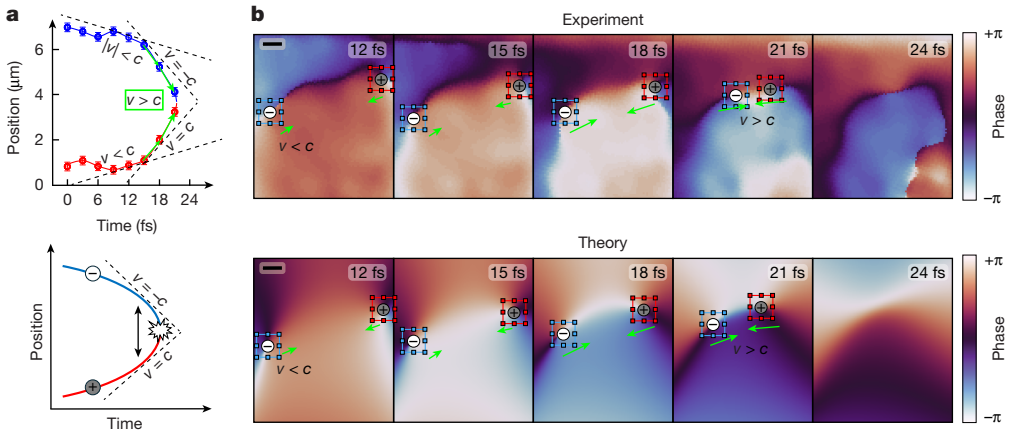

Fig. 2 | Deep sub-cycle annihilation of singularities, showing an example of acceleration towards formally divergent velocities along a characteristic space–time trajectory. a, The trajectories of oppositely charged singularities approaching annihilation form a closed, continuous curve in space–time, shown in experimental results (top) and illustration (bottom). In the moment before annihilation, any such continuous trajectory must approximate a parabolic curve, which necessarily contains a region in which the velocity of the singularity pair is divergent and consequently exceeds the speed of light (denoted by a dashed tangent). **b**, Measurement of singularity dynamics within 9 fs, focusing on the final frames before annihilation (top), in which the singularity dynamics appear as superluminal. Simulation based on the Gaussian random wave model (bottom), showing a qualitatively similar annihilation event. Scale bars, 1 μm.

ultraviolet regime (by fourth harmonic generation) and used to trigger the probe electrons in the UTEM. The rest of the pulse is downconverted (by difference frequency generation) to the mid-infrared range, corresponding to the upper Reststrahlen band of hBN supporting PhPs. The second path is used to pre-modulate the electrons at a reference sample. The third path generates the PhP wavepackets at the hBN sample. Details of the experimental scheme are provided in Extended Data Fig. 1 and Supplementary Information section I.

The reference and sample pulses can be tuned independently, allowing control over their relative sub-cycle (phase) delay $\Delta\phi$, intensity and polarization. The amplitude and phase at each frame are acquired by measuring multiple sub-cycle delays $\Delta\phi$ following the approach of FERI[25]. This way, we extract the phase and amplitude of the PhP near-field component pointing along the electron trajectory (Fig. 1b,c). See Supplementary Information section IV for more details. To image also the group dynamics of the PhP, we scan over the time delay Δt between the electron pulses and the light excitation of the sample. For each time delay, we reconstruct the amplitude and phase, enabling us to track the group dynamics of the field (Fig. 1d and Supplementary Information movie).

Each retrieved frame contains a complex interference pattern, involving phase singularities of right- and left-handed 2π winding, corresponding to positive or negative topological charge[7]. After aligning all the frames through computational reconstruction, we automate the identification of singularities, separating them by positive and negative topological charges (Extended Data Fig. 2, Supplementary Information section V). Analysing this extensive dataset, we also automate the tracking of the trajectories of the singularities, denoting their creation and annihilation events. By quantifying singularity positions and velocities over time, we analyse their statistical properties, specifically deriving their velocity distribution and joint distance–velocity distributions, constituting the full phase-space correlations.

A common framework for studying numerous properties of phase singularities and their correlations is the interference of Gaussian random 2D waves[5–7,36]. In our experiment, the rough boundaries of the hBN sample couple the incident laser into multiple PhP plane waves with arbitrary angles and phases. These waves then undergo multiple internal scattering at other boundaries, generating complex interference patterns, producing Gaussian random wave statistics. Despite its simplicity, the random-waves model captures a wide range of universal wave phenomena and applies to diverse experimental settings. Within this framework, the dynamics of the singularities is universal across different wave systems; only the parameters of their statistical distributions (such as the average velocity) depend on specific material properties such as wave dispersion and excitation properties such as the central wavelength λ_0 and standard deviation (bandwidth) $\Delta\lambda$. As we see below by comparing the theory with our experimental results, this model successfully describes many advanced features of PhP wavepackets in hBN. Moreover, the model holds even when we extend the theoretical analysis to predict the joint distance–velocity correlations, offering a complete characterization of singularity dynamics within their phase space.

Superluminal sub-cycle singularity-pair annihilation

The acceleration of opposite-charged singularities before annihilation or after creation is a universal feature in the interference of Gaussian random waves and can be understood through the space–time trajectories of annihilating singularities (Fig. 2a). As opposite-charged singularities approach each other, their paths in space–time must form a continuous curve at the annihilation point, forcing their acceleration to unbounded velocities right before the annihilation. This fact is a mathematical consequence of the continuity of the phase rather than a violation of physical laws. Phase singularities do not carry energy or information and thus can 'move' superluminally without breaking causality[12]; their apparent superluminal motion is a pure kinematic property of the evolving phase landscape. To better understand how singularities can move with unbounded velocities, we show a simple example of this phenomenon in Supplementary Information section XI.

The speed with which singularities move must be distinguished from other ubiquitous superluminal phenomena in optics[40], such as the well-known superluminal propagation of optical phase fronts[41] or the superluminal Rabi rotation of optical vortex cores[42]. Unlike the phase-front dynamics, for phase singularities, the unbounded velocities correspond to their universal space–time trajectories as they accelerate towards annihilation.

This acceleration of the singularities before annihilation is not unique to optical singularities and can, in principle, be observed in various physical systems. In superfluids, vortex–antivortex pairs accelerate towards each other before annihilating, with their velocity increasing sharply just before the collision. In superconductors, magnetic vortices and antivortices experience mutual attraction and accelerate rapidly before annihilation, producing a characteristic voltage peak. Similarly, in fluid dynamics, vortex rings can accelerate and deform as

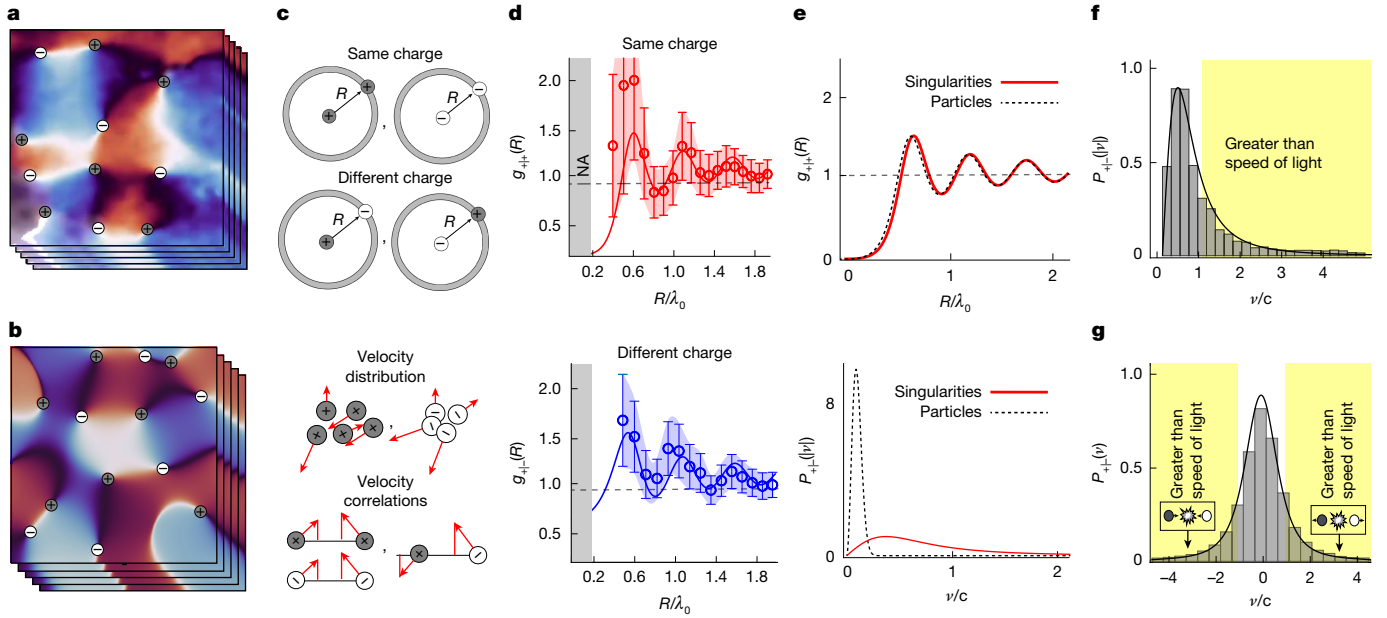

Fig. 3 | Distance correlations and velocity distributions of singularities. **a**, Experimentally measured phase of the PhP field in an hBN flake, displaying '+' and '−' singularities whose phase wraps by ±2π. **b**, Similar singularities appear in the phase of a simulated interfering Gaussian random waves. **c**, Definition of the distance correlation (top) for same-charge and different-charge pairs, and of velocity distribution and correlations (bottom). **d**, The distance correlation (top) of singularities resembles that of interacting particles that make up liquids[8], whereas the singularity velocities distribution (bottom) breaks this analogy, showing a large fraction of singularities that appear to move with superluminal velocities. Hence, although singularities share some particle-like properties, they remain a unique system. **e**, Theoretically predicted (solid lines) and experimentally measured (circles) distance correlation functions $g_{+|+}(R)$ and $g_{+|-}(R)$. The experimental data have larger error bars for small R because there are fewer events when singularities are at close distances to each other (see Supplementary Information section VI). NA denotes regions that do not contain enough singularities to generate trustworthy statistics. **f**, Theoretical and experimental singularity velocity distributions $P_{\pm}(|v|)$. The average velocity of the singularities is $\langle v\rangle = 3.12\times10^8\ \mathrm{m\,s^{-1}} \approx 1.04c$, where c is the speed of light in vacuum. Part of the singularities have velocities much higher than the speed of light. **g**, Theoretical and experimental relative velocity correlations show a good match. Unbounded negative velocities correspond to annihilation events, whereas unbounded positive velocities correspond to creation events.

they approach collision, exhibiting a burst of speed before merging or breaking apart. These examples stress that the characteristics of phase singularities are universal across different physical platforms, in optics and beyond. Although similar pre-annihilation acceleration has been observed in superfluids, superconductors and fluid vortices, in all these platforms, the velocities remained subluminal (Methods and Supplementary Information sections X and XI).

A large-scale statistical analysis of the measured singularities provided below helps identify what conditions made the optical PhP platform favourable for the observation of apparent superluminal dynamics. We monitor the entire sample area ($21\times21\ \mu\mathrm{m}^2$) over 800 ps, analysed in 285 phase-resolved frames (each created by 15 sub-cycle frames). An ensemble of about 50 singularities is tracked in each frame. This large dataset allows us to quantify the statistical properties and correlations among all singularity pairs: observing both their expected spatial correlations and previously inaccessible velocity correlations, which show universal properties in the collective dynamics of singularity ensembles.

Distance–velocity correlations in singularity ensembles

We compare simulations of the Gaussian random wave model with our experimental results by deriving distance and velocity correlation functions for singularities (Fig. 3a–c). Figure 3e presents the experimentally measured and theoretically predicted distance correlation functions for the same charge $g_{+|+}(R) = g_{-|-}(R)$ and opposite charge $g_{+|-}(R) = g_{-|+}(R)$. Each distance correlation function is defined as the probability density of finding a pair of singularities at separation distance R, normalized such that $g(R) = 1$ corresponds to the global average density, for the same or opposite charge[6,7]. The in-plane isotropy of hBN PhPs implies that the distance correlations depend only on the distance R with no dependence on the polar angle. The measured distance correlations $g_{+|+}$ and $g_{-|-}$ match the theoretical prediction of the Gaussian random wave model, with larger error bars at smaller distances because of the scarcity of events with small distances.

Figure 3d presents the ubiquitous particle analogy for singularities. As shown before[6], the distance correlation function resembles those of particles that make up a liquid (with average period of correlations about 0.3 nm)[8], exhibiting similar spatial short-range order because of their interactions. Going beyond the distance correlations, now we also measure the velocity distribution (Fig. 3f), as proposed in ref. 7. The velocity distribution has a distinct heavy tail. Specifically, comparing with the (Maxwell–Jüttner) velocity distribution of particles at the same relativistic temperatures (Fig. 3d, bottom) shows the unique behaviour of singularities ensembles; their heavier tails, as discussed in ref. 7, break the particle-singularity analogy.

The velocity distribution of phase singularities $P_{\pm}(|v|)$ is defined as the probability density of singularities to have absolute velocity $|v|$ (with $P_{+}(|v|) = P_{-}(|v|)$ due to symmetry):

$$P_{\pm}(|v|) = \int_0^{2\pi} P_{\pm}(v_x = |v|\cos\theta, v_y = |v|\sin\theta)|v|\,\mathrm{d}\theta \tag{1}$$

Furthermore, the velocity distribution can be calculated analytically[7], showing good agreement with the experimental results in Fig. 3f:

$$P_{\pm}(|v|) = \frac{8\pi^2\langle v\rangle^2|v|}{(\pi^2|v|^2 + 4\langle v\rangle^2)^2} \tag{2}$$

where $\langle v\rangle$ is the average velocity of the singularities. This value is calculated by averaging all the measured velocities of singularities in the

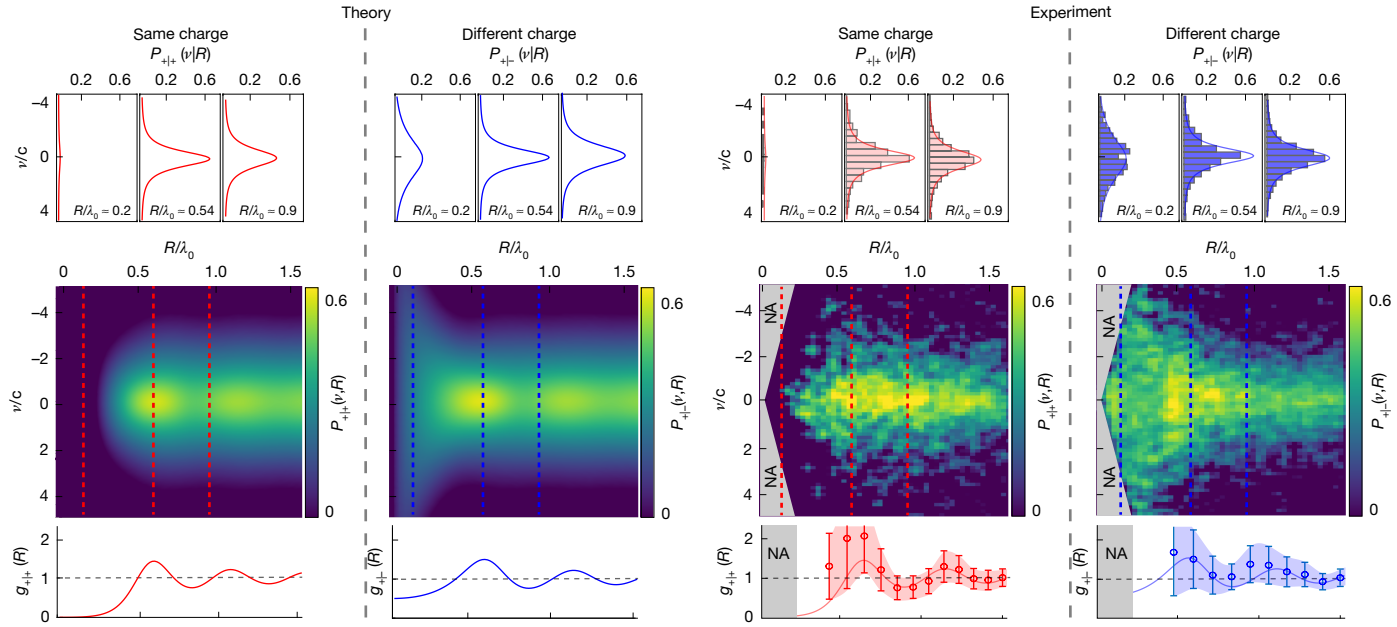

Fig. 4 | Full phase-space correlations of singularities. Plots of $P_{+|+}(v, R)$ and $P_{+|-}(v, R)$ as a function of both v and R show a good match between theory and experiment, revealing distinct behaviours. At proximity, same-charge singularities ($P_{+|+}(v, R)$) are uncommon. By contrast, for the same R values, opposite-charge singularities ($P_{+|-}(v, R)$) are more common and exhibit higher velocities, indicating acceleration before annihilation or after creation. Experimental results (right) align well with the theoretical model (left) of random wave interference. The bins of the experimental results hold a minimum of 50 singularity counts per bin. NA denotes regions in which not enough singularities were found to generate trustworthy statistics or in which the velocities were too high for detection.

experiment (the distance that the singularity travelled between frames, divided by time step) and is measured directly in our experiment to be $\langle v \rangle \approx (1.04 \pm 0.04)c$.

The measured $\langle v \rangle$ is in close agreement with the theoretical prediction[7]. The average velocity is given by $\langle v \rangle = c \cdot \pi/\sqrt{2}\,(1 + (\lambda_0/\Delta\lambda)^2\,(v_g/v_{ph})^2)^{-1/2}$, with v_{ph} and v_g being the average phase and group velocities of the PhPs (Supplementary Information section X). In hBN, the group velocity of PhPs is much smaller than the phase velocity over a broad-spectral range, with $v_{ph}/v_g \approx 12 \pm 1$ in our case, leading to a theoretical prediction of $\langle v \rangle \approx (1 \pm 0.1c)$, matching our measurement. This coincidence of having an average velocity so close to c further motivates the comparison of singularity velocities to the speed of light in Fig. 2.

This result also highlights a unique property of hBN PhPs: their slow group velocity enhances the variance of the wavevector distribution, thereby increasing the weight of extreme velocity singularities in the heavy tails of the distribution. This extended variance yields an average velocity that slightly exceeds the speed of light. In comparison, the average velocity would be much lower if not for the hyperbolic nature of hBN PhP. For instance, in free space, where $v_{ph} = v_g$, the average singularity velocity is an order of magnitude smaller $\langle v \rangle \approx 0.1c$. Consequently, only 0.4% of the singularities would exceed the speed of light, for the same laser parameters (analysis shown in Supplementary Fig. 4). By contrast, 29% of the singularities in our system exceed the speed of light, as shown by both data and theory in Fig. 3f. This comparison stresses that the example we provided in Fig. 2 is not exceptional, but very common in our experiment. Thus, the PhP platform makes it far more likely to observe the apparent superluminal events.

Full phase-space correlations in ensembles of singularities

We next extend the theory of singularities in Gaussian random waves. We first predict the characteristic velocity correlations among singularity pairs, for same-charge $P_{+|+}(v)$ and opposite-charge $P_{+|-}(v)$ singularities. Analytical analysis is presented in Supplementary Information sections VII–IX. These correlations represent the probability of two singularities having a relative velocity v along their connecting line:

$$P_{\sigma|\sigma'}(v) = \frac{1}{N_{\sigma\sigma'}} \left\langle \sum_{a\in\sigma, b\in\sigma'} \delta(v - (\mathbf{v}_a - \mathbf{v}_b)\cdot \mathbf{R}_{ab}) \right\rangle \quad (3)$$

where $\sigma,\sigma' \in \{+, -\}$ specify charge types, $N_{\sigma\sigma'}$ is the total number of pairs with these charges, $\hat{\mathbf{R}}_{ab}$ is a unit vector along the line connecting charge a with b and δ is the Dirac delta function. The brackets $\langle \ldots \rangle$ denote an average over all possible realizations. This definition leaves us with two distinct probabilities: same charge $P_{+|+} = P_{-|-}$ or opposite charges $P_{+|-} = P_{-|+}$.

Figure 3g presents $P_{+|-}(v)$, demonstrating good agreement with theory. The correlations become charge-independent ($P_{+|+}(v) = P_{+|-}(v)$) for large-enough sample sizes (shown in Supplementary Information section VII)—that is, analysis of the entire singularity ensemble remains unaffected by creation and annihilation events, which are rare. To capture the full dynamics of the singularities and especially pinpoint their behaviour close to annihilation and creation events, we next consider a more advanced correlation function.

Finally, we define the full phase-space correlations, described by the joint distance–velocity distribution that captures the evolution of the entire system:

$$P_{\sigma|\sigma'}(v, R) = \frac{1}{N_{\sigma\sigma'}(R)} \left\langle \sum_{a\in\sigma, b\in\sigma'} \delta(v - (\mathbf{v}_a - \mathbf{v}_b)\cdot \mathbf{R}_{ab})\delta(R - |\mathbf{r}_a - \mathbf{r}_b|) \right\rangle \quad (4)$$

$N_{\sigma\sigma'}(R)$ is the total number of pairs with charges $\sigma\sigma'$ separated by distance R. Symmetry considerations imply that $P_{+|+}(v, R) = P_{-|-}(v, R)$ and $P_{+|-}(v, R) = P_{-|+}(v, R)$.

Figure 4 presents both theoretical predictions (analytical results in Supplementary Information section IX) and experimental results obtained by analysis of the entire dataset, showing good agreement. The joint probabilities $P_{+|+}(v, R)$ and $P_{+|-}(v, R)$ generalize the analysis in previous works[7]: The distance correlations are reproduced once

integrating over v, and the velocity distributions are reproduced once integrating over R.

The joint distance–velocity distribution, defined by equation (4), can capture the singularity-pair creation and annihilation events. Figure 4 shows that at small distances ($R < \lambda_0$), the fraction of created and annihilated singularity pairs is large, leading to higher overall values of $P_{+|-}(v, R)$ and a wider variance, indicating higher possible velocities. The complementary $P_{+|+}(v, R)$ is smaller, because same-charge singularities are less likely at small distances, as expected by the known instability of singularities with charges higher than ±1 (refs. 36,37). At larger distances, singularities cannot be created or annihilated, resulting in narrower velocity distributions (see also Supplementary Fig. 3).

Finally, as the apparent velocities of phase singularities are formally divergent, their maximum observable value is limited by the state-of-the-art spatial and temporal microscopy resolution. Going beyond the current temporal resolution of few femtoseconds and spatial resolution of few tens of nanometres will enable observing singularity velocities orders of magnitude above c.

Conclusion and outlook

We experimentally observed dynamical correlations among ensembles of optical singularities in hBN, using ultrafast electron microscopy. Our measurements captured deep sub-cycle (3 fs ≈ T/8) creation and annihilation events of singularities with deep sub-wavelength resolution (20 nm ≈ λ_{PhP}/30). This combined resolution in time and space, in conjunction with the long interrogation time and large field of view, enabled us to demonstrate long-standing predictions about singularity velocity correlations and the possibility of unbounded velocities[7], a universal phenomenon for Gaussian random waves. The imaging abilities presented in this work motivated more advanced statistical analysis of dynamical correlation functions. Specifically, measuring the joint distance–velocity distributions showed the acceleration of oppositely charged singularities before annihilation and after creation.

The past decade has shown renewed interest in the superoscillatory[31,43] nature of certain wavefields—in which local field–phase gradients can exceed the maximum spatial frequency. Superoscillations arise near the centre of every phase singularity[44] and hold promise for advanced optical microscopy techniques with deep sub-wavelength resolution[30]. Our experiment observes simultaneously, and distinguishes, the two phenomena: (1) superoscillations are inherently created by phase singularities as seen at every frame and (2) the apparent superluminal velocities are observed in the dynamics between frames. There seems to be an indirect, yet intriguing, connection between these distinct features of topological defects, calling for further research. The extreme dynamics of singularities seem to be a direct manifestation of superoscillatory field gradients, once undergoing temporal evolution.

The experimental approach presented here could extend to the study of polaritons in other two-dimensional (2D) materials and their heterostructures, which would be particularly interesting in systems exhibiting highly tunable optical properties. Polaritonic properties of these materials include exotic topological phases and intricate coupling of the electric and magnetic fields, all suggesting intriguing changes in the singularity distributions and correlations. Materials with strong nonlinear optical responses could break the Gaussian random wave model and enable the generation of more complex interference patterns, potentially containing new types of singularity beyond the fundamental ±1 orders.

Future work that will probe higher-order and multi-dimensional singularities provide a larger and richer space for encoding information[45,46] corresponding to more intricate types of collective phenomena in the overall system. In that sense, our approach could be applied to study other topological phenomena, such as optical skyrmions[34], tracking their ultrafast dynamics and resolving their sub-cycle features. By using electron energy post-selection, we can further achieve orbital angular momentum selectivity[29]. Then, using an additional point of interaction for mixing different states of angular momentum will enable performing quantum tomography[47] of exotic topological states, such as quantum skyrmions[48].

This experiment studied the behaviour of singularity in 2D random Gaussian waves. In three dimensions, interference of random waves results in line singularities (for example, C lines[12]), continuous curves along which the phase is undefined. These singularity lines exhibit ultrafast motion and statistical correlations analogous to point singularities. Experimentally imaging these line singularities in the near field is extremely challenging because of the limitation of the present-day ultrafast transmission electron microscopes to measure only the field projection along one axis. Probing the richer space of three-dimensional (3D) singularities, and more generally 3D near-fields, requires developing tomographic reconstruction techniques in ultrafast electron microscopy[49].

Free electrons can not only probe the dynamics of singularities, but their wavefunctions can also be modified through interactions with these singularities. These interactions can imprint phase singularities onto electron wavefunctions, generating new electronic states[29,50], with potential applications in electron holography and other electron interference techniques.

Finally, the analytical approaches developed here could be leveraged to address long-standing challenges in electron microscopy, such as the fluctuating granularity or 'bee-swarm' effect[51,52]. By quantitatively mapping the dynamics of these fluctuations and analysing their ensemble-level correlations, we can devise mitigation strategies that push atomic-scale imaging beyond current limits.

Online content

Any methods, additional references, Nature Portfolio reporting summaries, source data, extended data, supplementary information, acknowledgements, peer review information; details of author contributions and competing interests; and statements of data and code availability are available at https://doi.org/10.1038/s41586-026-10209-z.

1. Embon, L. et al. Imaging of super-fast dynamics and flow instabilities of superconducting vortices. *Nat. Commun.* **8**, 85 (2017).
2. Sachkou, Y. P. et al. Coherent vortex dynamics in a strongly interacting superfluid on a silicon chip. *Science* **366**, 1480–1485 (2019).
3. Bliokh, K. Y. et al. Roadmap on structured waves. *J. Opt.* **25**, 103001 (2023).
4. Dennis, M. R., King, R. P., Jack, B., O'Holleran, K. & Padgett, M. J. Isolated optical vortex knots. *Nat. Phys.* **6**, 118–121 (2010).
5. Berry, M. V. Disruption of wavefronts: statistics of dislocations in incoherent Gaussian random waves. *J. Phys. A Math. Gen.* **11**, 27–38 (1978).
6. De Angelis, L., Alpeggiani, F., Di Falco, A. & Kuipers, L. Spatial distribution of phase singularities in optical random vector waves. *Phys. Rev. Lett.* **117**, 093901 (2016).
7. Berry, M. V. & Dennis, M. R. Phase singularities in isotropic random waves. *Proc. R. Soc. Lond. A* **456**, 2059–2079 (2000).
8. Hansen, J. P. & McDonald, I. R. *Theory of Simple Liquids: With Applications to Soft Matter* (Academic Press, 2013).
9. Toulouse, G. & Kléman, M. Principles of a classification of defects in ordered media. *J. Physique Lett.* **37**, 149–151 (1976).
10. Blatter, G., Feigel'man, M. V., Geshkenbein, V. B., Larkin, A. I. & Vinokur, V. M. Vortices in high-temperature superconductors. *Rev. Mod. Phys.* **66**, 1125–1388 (1994).
11. Drori, L. et al. Quantum vortices of strongly interacting photons. *Science* **381**, 193–198 (2023).
12. Sugic, D. et al. Particle-like topologies in light. *Nat. Commun.* **12**, 6785 (2021).
13. Indebetouw, G. Optical vortices and their propagation. *J. Mod. Opt.* **40**, 73–87 (1993).
14. Freund, I. Optical vortex trajectories. *Opt. Commun.* **181**, 19–33 (2000).
15. Li, P. et al. Hyperbolic phonon-polaritons in boron nitride for near-field optical imaging and focusing. *Nat. Commun.* **6**, 7507 (2015).
16. Yoxall, E. et al. Direct observation of ultraslow hyperbolic polariton propagation with negative phase velocity. *Nat. Photon.* **9**, 674–678 (2015).
17. Caldwell, J. D. et al. Photonics with hexagonal boron nitride. *Nat. Rev. Mater.* **4**, 552–567 (2019).
18. Kurman, Y. et al. Spatiotemporal imaging of 2D polariton wave packet dynamics using free electrons. *Science* **372**, 1181–1186 (2021).
19. Giles, A. J. et al. Ultralow-loss polaritons in isotopically pure boron nitride. *Nat. Mater.* **17**, 134–139 (2018).
20. Barwick, B., Flannigan, D. J. & Zewail, A. H. Photon-induced near-field electron microscopy. *Nature* **462**, 902–906 (2009).

21. Feist, A. et al. Quantum coherent optical phase modulation in an ultrafast transmission electron microscope. *Nature* **521**, 200–203 (2015).
22. Madan, I. et al. Holographic imaging of electromagnetic fields via electron-light quantum interference. *Sci. Adv.* **5**, eaav8358 (2019).
23. Nabben, D., Kuttruff, J., Stolz, L., Ryabov, A. & Baum, P. Attosecond electron microscopy of sub-cycle optical dynamics. *Nature* **619**, 63–67 (2023).
24. Gaida, J. H. et al. Attosecond electron microscopy by free-electron homodyne detection. *Nat. Photon.* **18**, 509–515 (2024).
25. Bucher, T. et al. Coherently amplified ultrafast imaging using a free-electron interferometer. *Nat. Photon.* **18**, 809–815 (2024).
26. Nye, J. F. & Berry, M. V. Dislocations in wave trains. *Proc. R. Soc. Lond. A* **336**, 165–190 (1974).
27. Nye, J. F. The motion and structure of dislocations in wavefronts. *Proc. R. Soc. Lond. A* **378**, 219–239 (1981).
28. Andersen, M. F. et al. Quantized rotation of atoms from photons with orbital angular momentum. *Phys. Rev. Lett.* **97**, 170406 (2006).
29. Tsesses, S. et al. Tunable photon-induced spatial modulation of free electrons. *Nat. Mater.* **22**, 345–352 (2023).
30. Török, P. & Munro, P. R. T. 2004. The use of Gauss-Laguerre vector beams in STED microscopy. *Opt. Express* **12**, 3605–3617 (2004).
31. Berry, M. et al. Roadmap on superoscillations. *J. Opt.* **21**, 053002 (2019).
32. Mair, A., Vaziri, A., Weihs, G. & Zeilinger, A. Entanglement of the orbital angular momentum states of photons. *Nature* **412**, 313–316 (2001).
33. Gibson, G. et al. Free-space information transfer using light beams carrying orbital angular momentum. *Opt. Express* **12**, 5448–5456 (2004).
34. Davis, T. J. et al. Ultrafast vector imaging of plasmonic skyrmion dynamics with deep subwavelength resolution. *Science* **368**, eaba6415 (2020).
35. Ni, J. et al. Multidimensional phase singularities in nanophotonics. *Science* **374**, eabj0039 (2021).
36. Berry, M. V. & Dennis, M. R. Knotted and linked phase singularities in monochromatic waves. *Proc. R. Soc. Lond. A* **457**, 2251–2263 (2001).
37. Ostrovsky, E., Cohen, K., Tsesses, S., Gjonaj, B. & Bartal, G. Nanoscale control over optical singularities. *Optica* **5**, 283–288 (2018).
38. Eckhardt, B., Dörr, U., Kuhl, U. & Stöckmann, H. J. Correlations of electromagnetic fields in chaotic cavities. *Europhys. Lett.* **46**, 134–140 (1999).
39. Dai, S. et al. Tunable phonon polaritons in atomically thin van der Waals crystals of boron nitride. *Science* **343**, 1125–1129 (2014).
40. Berry, M. V. Vector fields for monochromatic waves with general dispersion: vortex and stagnation singularities. *J. Phys. A Math. Theor.* **58**, 275201 (2025).
41. Vasnetsov, M., Pas' ko, V., Khoroshun, A., Slyusar, V. & Soskin, M. Observation of superluminal wave-front propagation at the shadow area behind an opaque disk. *Opt. Lett.* **32**, 1830–1832 (2007).
42. Dominici, L. et al. Full-Bloch beams and ultrafast Rabi-rotating vortices. *Phys. Rev. Res.* **3**, 013007 (2021).
43. Jordan, A. N., Howell, J. C., Vamivakas, N. & Karimi, E. Superoscillations and physical applications. In *Operator Theory* (eds Alpay, D. et al.) https://doi.org/10.1007/978-3-0348-0692-3_101-1 (Springer, 2025).
44. Berry, M. V. Waves near zeros. In *Proc. Conference on Coherence and Quantum Optics*, CMB1, OSA Technical Digest (CD) (Optica Publishing Group, 2007).
45. Zhao, Z. et al. Experimental demonstration of 16-Gbit/s millimeter-wave communications link using thin metamaterial plates to generate data-carrying orbital-angular-momentum beams. In *IEEE International Conference on Communications*, 1392–1397 (IEEE, 2015).
46. Stav, T. et al. Quantum entanglement of the spin and orbital angular momentum of photons using metamaterials. *Science* **361**, 1101–1104 (2018).
47. Gorlach, A. et al. Photonic quantum state tomography using free electrons. *Phys. Rev. Lett.* **133**, 250801 (2024).
48. Forbes, A., Nothlawala, F. & Vallés, A. Progress in quantum structured light. *Nat. Photon.* **19**, 1291–1300 (2025).
49. Shpiro, T. et al. Toward photon-induced near-field electron tomography. Preprint at https://arxiv.org/abs/2510.24648 (2025).
50. Bliokh, K. Y. et al. Theory and applications of free-electron vortex states. *Phys. Rep.* **690**, 1–70 (2017).
51. Midgley, P. A. & Dunin-Borkowski, R. E. Electron tomography and holography in materials science. *Nat. Mater.* **8**, 271–280 (2009).
52. Russo, C. J. & Henderson, R. Charge accumulation in electron cryomicroscopy. *Ultramicroscopy* **187**, 43–49 (2018).

Methods

Ultrafast transmission electron microscope

Experiments were performed in a pump–probe ultrafast transmission electron microscope based on a JEOL JEM-2100 Plus with a LaB6 electron gun operated at 200 kV (Extended Data Fig. 1a,b). The microscope was run in low-magnification mode (objective lens off) to keep the electron beam paraxial (convergence angle <1 mrad). Post-column electron energy loss spectrometer (EELS) (0.1 eV dispersion) provided energy filtering—a slit selected electrons that gained energy in both interactions. Images were recorded on a direct-detection camera (Gatan K2 Summit). The zero-loss peak full-width half maximum in vacuum was about 1.4 eV.

Laser system, optical paths and timing

A 40 W, 1,030 nm, about 270 fs, 1 MHz laser (Carbide) drove the pump–probe scheme. One branch was frequency-converted to 266 nm to photo-emit single-electron probe pulses at the LaB6 cathode. A second branch was difference-frequency-converted to the mid-infrared (around 7 μm) and split into two: one illuminated the sample and the other the reference interaction. Two delay stages controlled (1) the pump–probe delay for group-dynamics mapping and (2) a fine sub-cycle phase delay between reference and sample interactions. Mid-infrared pulses were transverse-magnetic-polarized and focused to approximately 100 μm (sample; 4–12 mW average power) and around 500 μm (reference; 4–20 mW). The sample path entered by a side port, and the sample was tilted by about 35° to avoid shadowing. The reference path impinged above the sample at about 20° with the reference membrane tilted by approximately 41° to satisfy phase matching with around 0.7c electrons.

Photonic electron–light modulator and energy-filtered imaging

The reference interaction used a modified Hard X-ray Aperture module carrying Si_3N_4 membranes (Extended Data Fig. 1c) coated with about 25 nm Al to implement a pre-sample photonic electron–light modulator (PELM)[53]. Electrons interacted first with the reference field and then with the sample field before energy selection and imaging. The average absorbed power at the sample was below the reported heating and damage thresholds for hBN[54].

Free-electron Ramsey imaging and phase retrieval

We used free-electron Ramsey imaging (FERI)[25] to reconstruct the complex near field at the sample. By scanning the relative optical phase between reference and sample interactions in sub-cycle steps, and by recording energy-filtered images, we retrieved amplitude and phase per pixel by an optimization-based forward model of the PINEM–FERI interaction (see Supplementary Information section IV for further details). In contrast to most phase-contrast imaging methods and phase retrieval methods in electron microscopy that rely on transverse coherence, FERI does not require transverse coherence at all. Instead, it relies on the longitudinal (temporal) energy modulation of the electron encoded through the PINEM interaction. This longitudinal modulation is a robust resource that is routinely achieved in UTEMs, as demonstrated by the widespread observation of PINEM sidebands[20,23–25,55–58].

Data acquisition, reconstruction and drift correction

We recorded 285 raw frames over about 855 fs with 3 fs sub-cycle sampling. Each amplitude/phase reconstruction used 15 sequential raw measurements; adjacent reconstructions overlapped by 14 frames to preserve temporal resolution. To correct mechanical and beam drift, we performed semi-automated feature extraction and applied affine transforms frame by frame before subsequent analysis (Extended Data Fig. 2). A linear interpolation produced a 0.2-fs-step movie for downstream singularity tracking.

Sample preparation

Isotopically pure $h^{11}BN$ crystals were grown as detailed in ref. 59, then mechanically exfoliated using low-retention PDMS (dry transfer). The flakes were transferred onto 20 nm SiN membranes (Norcada). Thicknesses of 40–50 nm were confirmed by EELS log-ratio analysis. The hBN flake covered most of the $21 \times 21\ \mu m^2$ field of view; sharp flake edges acted as near-field couplers for launching hyperbolic PhPs. For broader context on vortex dynamics in van der Waals platforms and 2D-material nanophotonics roadmaps relevant to hBN polaritons, see refs. 60–62.

Singularity identification, charge assignment and tracking

From the reconstructed phase maps, we located optical phase singularities by evaluating the 2π phase winding around pixel loops and assigned topological charge ±1. Connected-component clustering yielded singularity centroids for positive and negative charges. We enforced periodic boundary conditions when computing pair distances. Inter-frame association used a linear-assignment (Hungarian) approach with distance thresholds to obtain trajectories, creation and annihilation events; velocities were computed by finite differences along tracks. Our charge-assignment conventions and tracking of creation and annihilation events follow standard definitions for composite optical vortices and singular-skeleton evolution in time-dependent fields[63,64].

Distance correlations, velocity distributions and phase-space analysis

We computed same-charge and opposite-charge distance-correlation functions $g_{+|+}(r) = g_{-|-}(r)$ and $g_{+|-}(r) = g_{-|+}(r)$ as probability densities of finding singularity pairs at separation r, normalized by the averaged global density of singularities[7]. Velocity statistics included the singularity speed distribution $P(v)$ and relative-velocity correlations along the inter-singularity axis. To capture full dynamics, we evaluated the joint distance–velocity distribution $P(r, v)$, which marginalizes to $g(r)$ and $P(v)$. Experimental observables were compared with a theory of isotropic Gaussian random waves (non-monochromatic extension), for which we derived two-point correlators, including temporal derivatives and obtained $P(r, v)$ by Gaussian sampling of the joint distribution. The statistical framing and interpretation of pair interactions and correlations in singularity ensembles follows established treatments in random-wave and dispersive-wave settings[40,65–67].

Further derivations and validations are provided in the Supplementary Information.

Statistics and reproducibility

Distance and velocity distributions were aggregated over all reconstructions; uncertainties reflect finite-sample statistics, with larger error bars at small separations due to the scarcity of near-collision events. Regions without sufficient counts are marked as NA in the figures.

Estimating characteristic velocities and role of group velocity

The average velocity equals

$$\langle v \rangle = c \frac{\pi/\sqrt{2}}{\sqrt{1 + (\lambda_0/\Delta\lambda)^2 (v_g/v_{ph})^2}},$$

where the average wavelength is $\lambda_0 = 7\ \mu m$ and its standard deviation (bandwidth) is $\Delta\lambda = 0.3\ \mu m$ in the experiment. Owing to the unique property of PhPs in the sample to have a group velocity $v_g \ll v_{ph}$, we have $v_{ph}/v_g \approx 12 \pm 1$. This leads to the following average velocity:

$$\langle v \rangle \approx (1 \pm 0.1)c,$$

which is in very good agreement with the experimental result $\langle v \rangle \approx (1.04 \pm 0.004)c$. We want to emphasize that we achieved apparent superluminal velocities in the experiment because of the unique property of PhPs to have very slow group velocities. If the group velocity

were equal to the phase velocity, then we would have $\langle v \rangle \approx 0.1c$. However, owing to $v_{ph}/v_g \approx 12 \pm 1$, we get an average velocity higher than the speed of light c. Related discussions of topological-defect motion and apparent superluminality in other media can be found in refs. 68–70.

Image processing and software

All detector-level processing was disabled; raw camera data were exported and processed with in-house MATLAB code implementing the FERI forward model, phase retrieval, drift correction, singularity detection and tracking, and correlation analyses. Pseudocode for algorithms 1–3 (singularity detection, clustering and tracking/velocity extraction) is provided in the Supplementary Information.

Additional background and application

The broader context for vortex–defect analogies across platforms, historical foundations and structured-wave applications is discussed in refs. 71–84.

Data availability

The data supporting the findings of this study are available from the corresponding authors upon reasonable request.

53. Ferrari, B. M. et al. Realization of a pre-sample photonic-based free-electron modulator in ultrafast transmission electron microscopes. *ACS Photon.* **12**, 5864–5873 (2025).
54. Wu, Y. et al. Enhanced thermal conduction by surface phonon-polaritons. *Sci. Adv.* **6**, eabb4461 (2020).
55. Piazza, L. et al. Simultaneous observation of the quantization and the interference pattern of a plasmonic near-field. *Nat. Commun.* **6**, 6407 (2015).
56. Wang, K. et al. Coherent interaction between free electrons and a photonic cavity. *Nature* **582**, 50–54 (2020).
57. Kfir, O. et al. Controlling free electrons with optical whispering-gallery modes. *Nature* **582**, 46–49 (2020).
58. Bucher, T. et al. Free-electron Ramsey-type interferometry for enhanced amplitude and phase imaging of nearfields. *Sci. Adv.* **9**, eadi5729 (2023).
59. Liu, S. et al. Single crystal growth of millimeter-sized monoisotopic hexagonal boron nitride. *Chem. Mater.* **30**, 6222–6225 (2018).
60. Kurman, Y. et al. Dynamics of optical vortices in van der Waals materials. *Optica* **10**, 612–618 (2023).
61. Gibertini, M., Koperski, M., Morpurgo, A. F. & Novoselov, K. S. Magnetic 2D materials and heterostructures. *Nat. Nanotechnol.* **14**, 408–419 (2019).
62. de Abajo, F. J. G. et al. Roadmap for photonics with 2D materials. *ACS Photon.* **8**, 3961–4095 (2025).
63. Maleev, I. D. & Swartzlander, G. A. Jr. Composite optical vortices. *J. Opt. Soc. Am. B* **20**, 1169–1176 (2003).
64. Bekshaev, A., Chernykh, A., Khoroshun, A. & Mikhaylovskaya, L. Singular skeleton evolution and topological reactions in edge-diffracted circular optical-vortex beams. *Opt. Commun.* **397**, 72–83 (2017).
65. De Angelis, L., Alpeggiani, F., Di Falco, A. & Kuipers, L. Persistence and lifelong fidelity of phase singularities in optical random waves. *Phys. Rev. Lett.* **119**, 203903 (2017).
66. De Angelis, L. & Kuipers, L. Effective pair-interaction of phase singularities in random waves. *Opt. Lett.* **46**, 2734–2737 (2021).
67. Berry, M. V. Regular and irregular semiclassical wavefunctions. *J. Phys. A Math. Gen.* **10**, 2083–2092 (1977).
68. Kourkoulou, I., Landry, M. J., Nicolis, A. & Parmentier, K. Apparently superluminal superfluids. *J. High Energy Phys.* **2024**, 80 (2024).
69. Seo, S. W., Ko, B., Kim, J. H. & Shin, Y. I. Observation of vortex-antivortex pairing in decaying 2D turbulence of a superfluid gas. *Sci. Rep.* **7**, 4587 (2017).
70. Green, S. *Fluid Vortices* (Springer, 2012).
71. Fiorino, M. & Elsberry, R. L. Some aspects of vortex structure related to tropical cyclone motion. *J. Atmos. Sci.* **46**, 975–990 (1989).
72. Poincaré, H. Sur les courbes définies par les équations différentielles. *J. Math. Pures Appl.* **4**, 167–244 (1885).
73. Vanacore, G. M. et al. Author Correction: Attosecond coherent control of free-electron wave functions using semi-infinite light fields. *Nat. Commun.* **10**, 1069 (2019).
74. Machado, F., Rivera, N., Buljan, H., Soljačić, M. & Kaminer, I. Shaping polaritons to reshape selection rules. *ACS Photon.* **5**, 3064–3072 (2018).
75. Session, D. et al. Optical pumping of electronic quantum Hall states with vortex light. *Nat. Photon.* **19**, 156–161 (2025).
76. Spektor, G. et al. and Meyer zu Heringdorf, F.J. Revealing the subfemtosecond dynamics of orbital angular momentum in nanoplasmonic vortices. *Science* **355**, 1187–1191 (2017).
77. Lim, S. W. D., Spaegele, C. M. & Capasso, F. Multidimensional optical singularities and their applications. Preprint at https://arxiv.org/abs/2406.00784 (2024).
78. Thompson, W. *On Vortex Atoms* by Lord Kelvin. *Proc. R. Soc. Edin.* **6**, 94–105 (1867).
79. Zhang, Z. et al. Particlelike behavior of topological defects in linear wave packets in photonic graphene. *Phys. Rev. Lett.* **122**, 233905 (2019).
80. Rumi, G. et al. Hyperuniform vortex patterns at the surface of type-II superconductors. *Phys. Rev. Res.* **1**, 033057 (2019).
81. Brandt, E. H. Electric field in superconductors with rectangular cross section. *Phys. Rev. B* **52**, 15442 (1995).
82. Aharonov, Y., Popescu, S. & Rohrlich D. How can an infra-red photon behave as a gamma ray? Preprint TAUP, 1847–1890 (1991).
83. Berry, M. V. in *Quantum Coherence and Reality: In Celebration of the 60th Birthday of Yakir Aharonov* (eds Anandan, J. S. & Safko, J. L.) 55–64 (World Scientific, 1994).
84. Rogers, E. T. et al. A super-oscillatory lens optical microscope for subwavelength imaging. *Nat. Mater.* **11**, 432–435 (2012).

Acknowledgements We warmly thank M. V. Berry for stimulating and insightful discussions, and Y.-N. Li for valuable discussions that significantly contributed to this work. This research was funded by the Gordon and Betty Moore Foundation (grant no. GBMF11473). This project was also funded by the ERC COG, QinPINEM of the European Union (project no. 101125662). We acknowledge funding from the Helen Diller Quantum Center. This work is part of the SMART-electron project, which received funding from the Horizon 2020 Research and Innovation Programme of the European Union (grant agreement no. 964591). S.T. acknowledges support from the Adams fellowship of the Israeli Academy of Science and Humanities, the Yad Hanadiv foundation through the Rothschild fellowship, the VATAT-Quantum fellowship by the Israel Council for Higher Education, the Helen Diller Quantum Center post-doctoral fellowship and the Technion Viterbi fellowship. E.J. and J.H.E were supported by the Office of Naval Research (award no. N00014-20–1-2474). C.R.-C. was funded by a Stanford Science Fellowship. K.W. was supported by the National Natural Science Foundation of China (no. 12374321), the Shanghai Rising-Star Program (no. 22QA1410100) and the international partnership of the Chinese Academy of Sciences (111GJHZ2022024FN). H.H.S. acknowledges support from ISF (grant no. 2576/25). A.G. acknowledges financial support from the Azrieli Foundation through the Azrieli Graduate Studies Scholarship. The experiments were performed on the UTEM of the AdQuanta group of I.K., which is installed in the Electron Microscopy Center (EMC) of the Department of Materials Science and Engineering at the Technion. We thank Integrated Dynamic Electron Solutions (IDES) Inc. for the support, advice and discussions. I.K. wholeheartedly acknowledges the support of R. Magid and B. Magid, whose donation made the purchase of the UTEM possible; without their help, all the experiments presented here would not have been possible.

Author contributions H.H.S. performed the sample fabrication. E.J. and J.H.E. grew the hBN crystals. A.N., H.N., K.W., Y.A., M.Y. and T.L.A. performed the measurements. A.G., Q.Y., R.R. and T.B. developed the theory. T.B., C.S., C.R.-C. and A.G. performed the analysis. T.B. performed the algorithm development. T.B., H.H.S., K.W., A.N., S.T., Y.A., M.Y., G.M.V. and I.K. designed the experiment. F.H.L.K, G.M.V., S.T. and I.K. supervised the work. All authors contributed to the analysis, discussion and writing of this work.

Competing interests The authors declare no competing interests.

Additional information

Supplementary information The online version contains supplementary material available at https://doi.org/10.1038/s41586-026-10209-z.

Correspondence and requests for materials should be addressed to I. Kaminer.

Peer review information *Nature* thanks Oleg Angelsky, Francesco Caravelli, Alexander Vernon and Claudia Zenkova for their contribution to the peer review of this work. Peer reviewer reports are available.

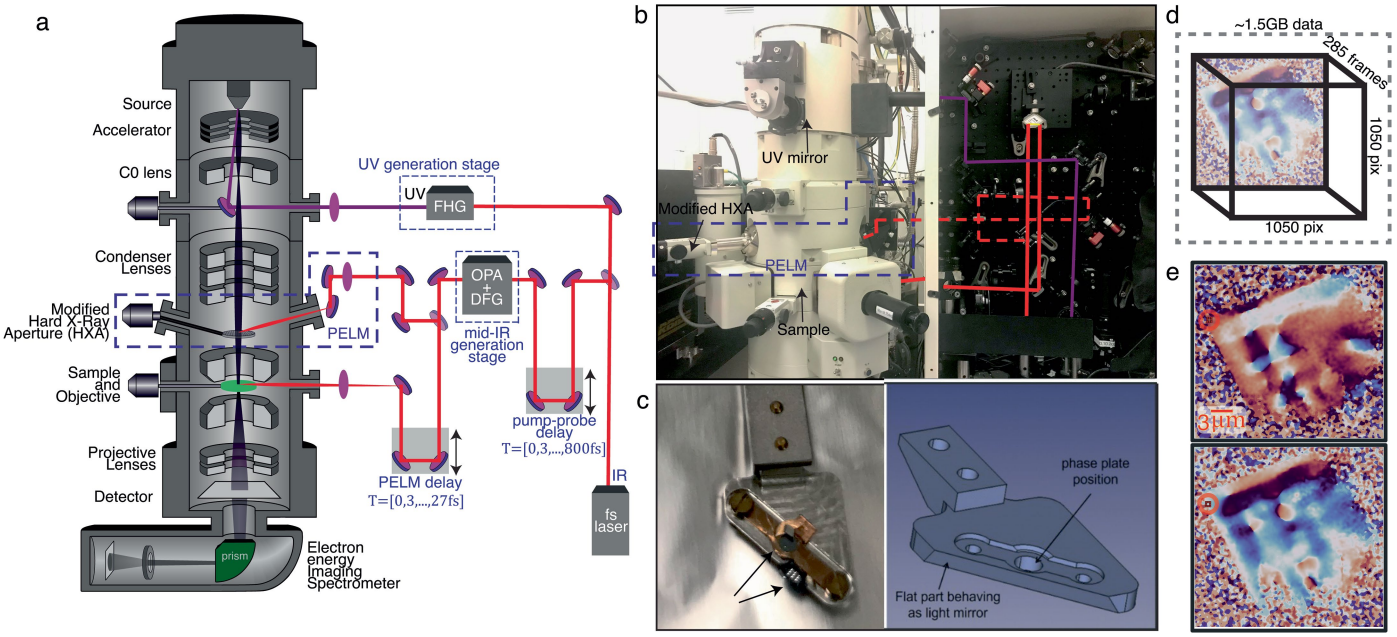

Extended Data Fig. 1 | The UTEM setup and the PELM integration. UTEM illustration (**a**) and image (**b**) illustrating the microscope column, electron spectrometer and detectors, optical setup, and the integration of a modified Hard X-ray Aperture (HXA) at a post-condenser lens stage (PELM). The external knob of the HXA (a and b, left side) has two rigid positioning points with 5 mm lateral travel around them for positioning the reference interaction point with respect to the electron beam path. An electron-transparent thin film sits at the place of the x-ray aperture, and light enters from the optical access port on the opposite side of the column at a 20-degree angle above the horizon (dashed red line in b). Double illumination scheme (a and b, right side) implemented on the vertical board next to the UTEM. The IR laser beam is separated into two portions using a 50:50 beam splitter. One portion is guided towards the PELM (dashed red line in b), whereas the other portion is guided towards the sample (solid red line in b). (**c**) Image (left) and CAD model (right) of the modified HXA aperture connected to the platelet hosting the electron-transparent light-opaque metallic thin films for electron-light interaction. The platelet is made of Aluminum alloy, whereas the clamp is made of 0.15-mm-thick Beryllium Copper. One can observe two Si-window TEM grids (Norcada Inc.), which are coated with a 25-nm-thick Aluminum film deposited via thermal evaporation on a 10-nm-thick Si_3N_4 membrane. In each grid, nine slots are present to maximize the available points of interaction in case of local damage to one of the membranes. The platelet has also been cut at a specific angle, allowing it to host a small metallic mirror able to reflect the light down the column towards the sample position (not used in the current work). The platelet, HXA, and their integration were designed and performed in close collaboration with IDES, part of JEOL Ltd. (**d**) By using the pump-probe delay stage in combination with the PELM delay stage, the setup allows a very long acquisition time in high spatiotemporal resolution with a large field of view. The result is 285 frames of 1050 × 1050 pix images, a total size of ~1.5GB of data to analyze with our specialized algorithmic process. (**e**) The very long acquisition time also results in sample and beam instability, which needs to be taken into account.

Extended Data Fig. 2 | Correcting sample and beam drift. Left: phase reconstructions for two different times (t_1, t_2), each time has a different rotation and translation, which is fixed by calculating an affine transformation from at least 10 features selected manually on each frame. Right: corresponding fixed phase reconstruction. The red circle marks the same pixel indices, which points on different coordinates on the sample for different times before the correction (left). After correction, the rectangle marks the same coordinates on the sample.